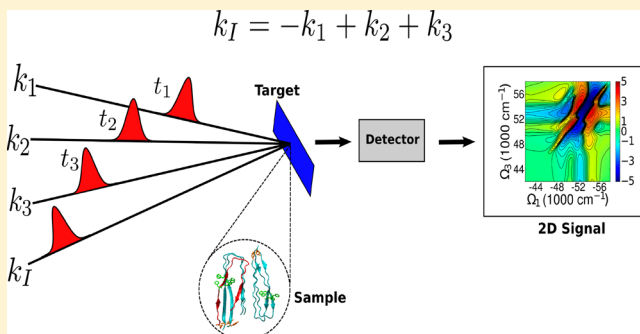


Tracking the Mechanism of Fibril Assembly by Simulated Two-Dimensional Ultraviolet Spectroscopy

A. R. Lam,^{*,†} J. J. Rodriguez,[†] A. Rojas,[‡] H. A. Scheraga,[§] and S. Mukamel[†][†]Department of Chemistry, University of California—Irvine, Irvine, California 92697-2025, United States[‡]Department of Biostatistics and Computational Biology, University of Rochester School of Medicine and Dentistry, Rochester, New York 14642-0001, United States[§]Baker Laboratory of Chemistry and Chemical Biology, Cornell University, Ithaca, New York 14853-1301, United States

Supporting Information

ABSTRACT: Alzheimer's disease (AD) is a neurodegenerative disorder characterized by the accumulation of plaque deposits in the human brain. The main component of these plaques consists of highly ordered structures called amyloid fibrils, formed by the amyloid β -peptide ($A\beta$). The mechanism connecting $A\beta$ and AD is yet undetermined. In a previous study, a coarse-grained united-residue model and molecular dynamics simulations were used to model the growth mechanism of $A\beta$ amyloid fibrils. On the basis of these simulations, a dock/lock mechanism was proposed, in which $A\beta$ fibrils grow by adding monomers at either end of an amyloid fibril template. To examine the structures in the early time-scale formation and growth of amyloid fibrils, simulated two-dimensional ultraviolet spectroscopy is used. These early structures are monitored in the far ultraviolet regime ($\lambda = 190–250$ nm) in which the computed signals originate from the backbone $n\pi^*$ and $\pi\pi^*$ transitions. These signals show distinct cross-peak patterns that can be used, in combination with molecular dynamics, to monitor local dynamics and conformational changes in the secondary structure of $A\beta$ -peptides. The protein geometry-correlated chiral $xxxx$ signal and the non-chiral combined signal $xyxy$ – $xyyx$ were found to be sensitive to, and in agreement with, a dock/lock pathway.



1. INTRODUCTION

Alzheimer's disease (AD) is a neurodegenerative disorder whose pathology is associated with the formation and deposition of amyloid plaques and fibrils in the brain.^{1,2} Amyloid plaques contain highly ordered forms of a protein known as the β -amyloid peptide ($A\beta$) which originates by cleavage of a large and multifunctional membrane protein called amyloid precursor protein (APP). $A\beta$ peptides are normally present in the body, predominantly in two alloforms, $A\beta_{(1-40)}$ and $A\beta_{(1-42)}$, with the latter having two additional amino-acid residues at the C-terminus. The neurotoxicity of the $A\beta$ peptides has been linked to their ability to form β -sheet structures and aggregates rather than to the amyloid plaques and fibrils themselves.^{3–7}

It has been reported that small fragments derived from $A\beta$ -peptide also form amyloid fibrils and can be crystallized,⁸ revealing important features that are believed to also be present in the fibrils formed by the parent peptides.⁹ Colletier and co-workers¹⁰ used a set of amyloid fragments composed of 6–7 residues and found that these fragments have the tendency to crystallize in different polymorphic oligomers with a variety of lifetimes and toxicity levels, which reveals that $A\beta$ -peptides may have a repertoire of accessible fibril structures. However,

neither of the full length peptides, $A\beta_{(1-40)}$ or $A\beta_{(1-42)}$, has been crystallized.

Because of their rapid aggregation and their propensity to assume different geometrical shapes, it is difficult to reveal the conformations of the $A\beta$ -peptides in aqueous solution. Crescenzi and co-workers¹¹ determined a three-dimensional structure of the $A\beta_{(1-42)}$ monomer by using CD and 2D NMR techniques in different media that mimic the lipid phase of membranes. The reported structure consists of two α -helices in which one of the helices, $A\beta_{(28-38)}$, corresponds to the transmembrane region of APP. Tycko et al. used solid state NMR techniques to study $A\beta_{(1-40)}$ fibrils and determined that these fibrils can assume different geometrical arrangements.^{12–16} On the basis of the constraints imposed by their solid state NMR data, they proposed geometrical models for wild-type $A\beta_{(1-40)}$ and Iowa mutant $A\beta(D23N)$. According to these models, $A\beta_{(1-40)}$ fibrils are formed by the stacking of U-shaped monomers held together by intermolecular hydrogen bonds. A quenched hydrogen/deuterium exchange NMR study by Lührs and co-workers¹⁷ resulted in a three-dimensional

Received: October 12, 2012

Revised: November 30, 2012

Published: December 7, 2012

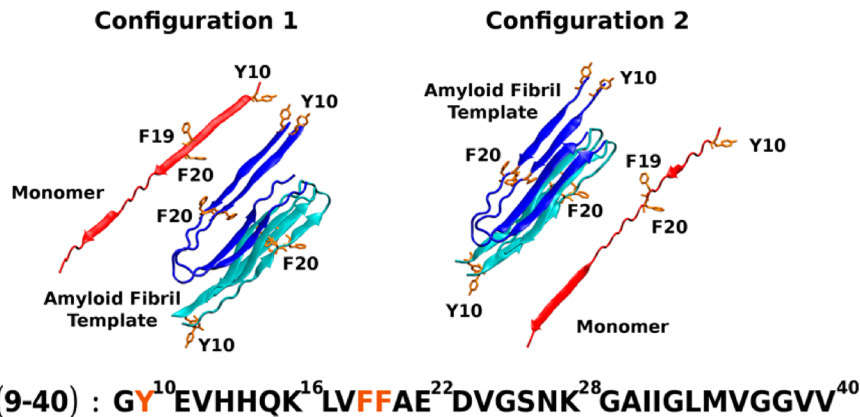


Figure 1. Initial Configurations taken from Rojas et al.⁴⁷ The $\text{A}\beta_{(9-40)}$ monomer (ribbon in red) is 20 Å away from the amyloid fibril template composed of two β -sheets of two $\text{A}\beta$ monomers each (in navy and blue, respectively). The primary sequence of $\text{A}\beta_{(9-40)}$ is displayed below the figures with the aromatic residues Tyr and Phe indicated in orange. Each monomer has one Tyr (Tyr10) and two Phe (Phe19 and Phe20) residues.

structure of the $\text{A}\beta_{(1-42)}$ amyloid fibrils that is similar to that reported by Tycko and co-workers.

In addition to the efforts made to understand the stability of $\text{A}\beta$ oligomers and fibrillar or nonfibrillar aggregates, considerable attention has been paid to the different pathways leading to the formation of $\text{A}\beta$ oligomers and their evolution into highly ordered amyloid fibrils.^{18–28} Bitan et al.²² determined that $\text{A}\beta_{(1-42)}$ peptides have a higher propensity to form larger oligomers than $\text{A}\beta_{(1-40)}$ peptides. Lim and co-workers²⁹ found that $\text{A}\beta_{(1-42)}$ monomers have a higher tendency to form β -strand conformations than $\text{A}\beta_{(1-40)}$ monomers. Jarret et al.^{30,31} reported that the C-terminus plays a critical role in the amyloidogenesis process. Despite these results, the growth mechanism of amyloid fibrils and the stage in which the oligomers become neurotoxic leading to AD is still an open issue.

Simulating fibril formation at the all-atom level is not possible with the computational resources available today. To reduce the computational cost, studies usually focus on fragments of $\text{A}\beta$ -peptides.^{32–35} Simulations of the full-length $\text{A}\beta$ -peptides have also been reported,^{36–40} but they are usually combined with coarse-grained models,^{36,37,39} implicit solvent,^{38,40} or the replica exchange method⁴¹ to speed up the computations. These studies provide some understanding of the conformational changes that $\text{A}\beta$ -peptides undergo when transitioning from a disordered to a highly ordered structure but do not fully reflect the true dynamics of the full-length $\text{A}\beta$ -peptide folding and aggregation.

Esler et al.³² used radiolabeled $\text{A}\beta$ -peptides to model the amyloid growth and concluded that the deposition of soluble $\text{A}\beta$ onto amyloid fibrils has two distinguishable kinetic steps: A reversible step in which an $\text{A}\beta$ monomer docks onto an amyloid template and an irreversible lock step in which an $\text{A}\beta$ monomer fully associates with the amyloid fibril. Cannon et al.⁴³ used surface plasmon resonance biosensors to study the kinetics associated with the early stage of β -amyloid fibril elongation and concluded that a peptide association/dissociation mechanism occurred in multiple steps. The soluble peptide first binds reversibly to the growing amyloid fibril and, in subsequent steps, the bound $\text{A}\beta$ peptide is stabilized into the growing fibril through postbinding transitional events. This step-by-step mechanism observed in fibril elongation was described theoretically by Massi and Straub⁴⁴ by using a schematic energy landscape with loosely defined reaction

coordinates and transition states for peptide/fibril association and reorganization. Their model incorporated different possible channels for peptide deposition, which included fast deposition from solution through an activation/nucleation event, and deposition of peptide from solution onto existing fibrils followed by reorganization of the peptide/fibril deposit. Nguyen et al.⁴⁵ proposed a dock/lock mechanism using the $\text{A}\beta_{(16-22)}$ fragment. Initially, in the first stage (docking), the $\text{A}\beta_{(16-22)}$ monomer increases its β -strand content while it docks onto a preformed oligomer. Subsequently, a slow lock-phase occurs, and the monomer rearranges to form in-register anti-parallel structures. O'Brien et al.⁴⁶ used simulations with an implicit solvent model and all-atom molecular dynamics in explicit water to study the thermodynamics of the dock-lock mechanism and showed that a locked full length monomer exhibited large conformational fluctuations when interacting with the underlying fibril.

Rojas et al.⁴⁷ used a coarse-grained united-residue (UNRES) model and replica-exchange molecular dynamics (REMD) simulations to model the assembly of a free and unrestrained $\text{A}\beta_{(9-40)}$ monomer onto a fibril template based on Tycko's $\text{A}\beta$ wild-type fibril model. They simulated the $\text{A}\beta_{(9-40)}$ assembly process and found that hydrophobic interactions and hydrogen bonds play a leading role in stabilizing the structures. The entire process follows a common dock/lock mechanism reaching two-locking states at the molecular level that agree with experiments on $\text{A}\beta$ monomer deposition.^{42,43}

Two-dimensional infrared (2DIR) optical spectroscopy has recently been applied to characterize protein structure and monitor fast folding processes.^{48–53} Sequences of laser pulses are used to excite vibrational states and the correlations between evolution in two controlled time intervals are determined. These are displayed in a two-dimensional map that reveals electronic and vibrational fluctuations in the ultrafast regime providing information about the molecular dynamics (MD). Two-dimensional ultraviolet spectroscopy (2DUV) is a natural extension of 2DIR. In recent years, the development of 2DUV experimental protocols for application to fast biochemical processes such as the interaction between DNA bases has proven that this novel technique is suitable for characterization of dynamical properties not observed with traditional techniques.^{54,55} Simulations of applied 2DUV spectroscopy showed that this technique can be used to characterize and distinguish secondary structures of pro-

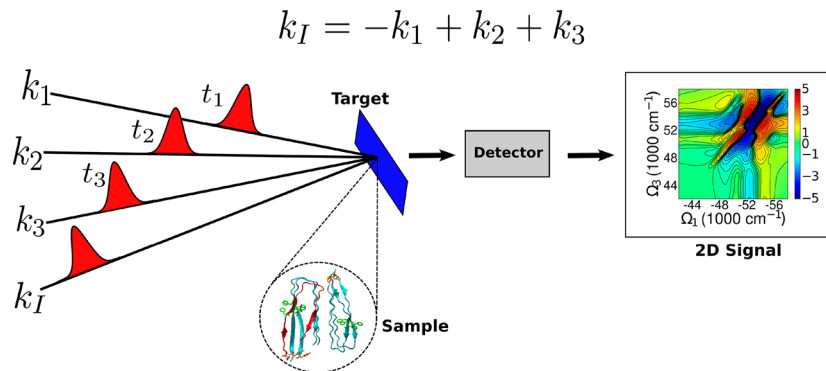


Figure 2. Configuration of pulses for a multidimensional four-laser mixing experiment. Three laser pulses with wave vectors k_1 , k_2 , and k_3 (in their respective chronological order, t_1 , t_2 , and t_3) interact with a target (a peptide or complex of peptides). A coherent signal field, $k_I = -k_1 + k_2 + k_3$, is also generated to enhance the output of the time-interval dependent signal $S(t_3, t_2, t_1)$ that carries information about the interactions and intensity changes and is collected by a detector. The signal is displayed as the two-dimensional Fourier transform of the times $t_1 \rightarrow \Omega_1$ and $t_3 \rightarrow \Omega_3$.

teins^{56,57} and highly ordered structures such as $\text{A}\beta$ -amyloid fibrils.^{58,59}

The purpose of the present study is to demonstrate how the 2DUV signals, calculated from the conformational changes in the protein geometry, obtained from the simulated UNRES trajectories,⁴⁷ may be used to monitor the assembly mechanism of an $\text{A}\beta$ -peptide monomer into an amyloid fibril template, and obtain structural information at early events (over a time scale of 20 ns). Correlation between these calculated signals and the simulated conformational changes that the $\text{A}\beta$ -peptide monomer exhibits during the assembly process are discussed.

2. THEORETICAL METHODS

Rojas et al. performed REMD simulations of the binding of an $\text{A}\beta$ peptide to an amyloid fibril template. Technical details of the force field and protein model used in the simulations are given in refs 47 and 60. The simulation setup is described as follows: A free and unrestrained single extended $\text{A}\beta$ -peptide monomer is initially placed 20 Å away from the amyloid fibril template. Due to an asymmetry in the configuration adopted by the $\text{A}\beta$ peptides, the opposite ends of a fibril are different. At one end, the N-terminal region is more exposed, and at the other, it is the C-terminal region that is left exposed. Therefore, to explore the possibility that the two ends may differ in binding modes, two initial configurations were prepared: in configuration 1, the extended monomer faces the N-terminal strands of the amyloid fibril template, whereas in configuration 2, it faces the C-terminal strands (Figure 1). The time evolution of configurations 1 and 2 was shown in Figures 7 and 8, respectively, of ref 47. Each of these two figures displays six representative conformations at different times at which a single $\text{A}\beta$ monomer starts to bind and finally docks onto a template. For each of the six representative conformations, a set of 100 snapshots were recorded at intervals of 121 fs. These coarse-grained snapshots were converted into all-atom conformations, and were used to simulate the corresponding 2DUV signals.

The 2DUV simulation protocol was described elsewhere.⁶¹ It uses a quantum mechanics/molecular mechanics computational approach based on the Frenkel exciton Hamiltonian with the electrostatic fluctuations algorithm (EHEF). The Hamiltonian that describes the interactions among all the electronic transitions has the form

$$\hat{H}_{\text{EHEF}} = \sum_{m_e} \varepsilon_{m_e}^{(i)} \hat{B}_{m_e}^\dagger \hat{B}_{m_e} + \sum_{m_e, n_f} J_{m_e, n_f}^{(i)} \hat{B}_{m_e}^\dagger \hat{B}_{n_f} \quad (1)$$

where m and n denote the amino-acid residues, e and f denote the excited and the final states of the transition (either $n\pi^*$ or $\pi\pi^*$) of the amino-acid unit, i denotes the snapshot index, $\varepsilon_{m_e}^{(i)}$ is the energy of the transition state for the m th residue in snapshot i . $\hat{B}_{m_e}^\dagger$ and \hat{B}_{m_e} are the exciton creation and annihilation operators, respectively, with the commutation relation $[\hat{B}_{m_e}, \hat{B}_{n_f}^\dagger] = \delta_{mn}(1 - 2\hat{B}_{m_f}^\dagger \hat{B}_{m_e})$. $J_{m_e, n_f}^{(i)}$ denotes the resonant coupling of the transitions in two amino-acid residues in the approximate form

$$J_{m_e, n_f}^{(i)} = \frac{1}{4\pi\varepsilon_0} \sum_{m_e} \sum_{n_f}^{n \neq m} \frac{Q_{m_e}^{\text{eg}} Q_{n_f}^{\text{gf}}}{|r_{m_e} - r_{n_f}|} \quad (2)$$

where ε_0 is the electric permittivity in vacuo, g denotes the ground state, and Q_m and r_m denote the charges and position of the m th residue. Diagonalization of the Hamiltonian of eq 1 yields the exciton eigenstates, and the nonlinear optical signals of the $\text{A}\beta$ assembly are computed by using the procedure given in ref 61 and implemented in the SPECTRON software package.

The UV linear absorption (LA), circular dichroism (CD), and 2DUV photon echo of the assembly are obtained by averaging over a set of MD snapshots. With the aid of the Hamiltonian of eq 1, the LA signal contains the eigenvalues and eigenstates of the protein, but not the geometry. The CD signal provides the distribution of the relative orientations of the dipole moments, i.e., the relative orientations of the amino-acid residues, and hence can identify secondary structures. 2DUV signals provide the information from LA and CD signals, and also the interactions between specific i and j dipole moments, i.e., between specific amino-acid residues. The DichroCalc software package⁶² was used to compute the LA and CD signals from the trajectories of ref 47.

The 2DUV photon echo signal technique uses three laser pulses with wave vectors k_1 , k_2 , and k_3 (in their respective chronological order, t_1 , t_2 , and t_3) that interact with the target (a peptide or complex of peptides). A coherent signal field, $k_I = -k_1 + k_2 + k_3$, is also generated with a time-interval-dependent signal $S(t_3, t_2, t_1)$ that carries information about the interactions and intensity changes of the oscillator fields of the system. The signals are displayed as the two-dimensional Fourier transform

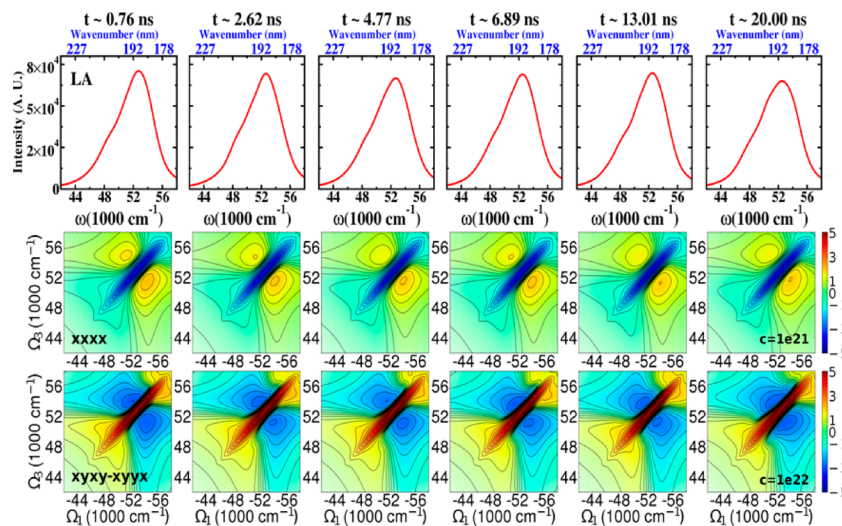


Figure 3. 1D and 2D spectra in the FUV regime for configuration 1 at different simulation times. **Top:** linear absorption (1D). **Middle:** 2D non-chiral xxxx spectra. **Bottom:** 2D non-chiral combination xyxy-xyyx signal. The non-chiral xxxx spectra have extended blue peaks at $52\ 000\ \text{cm}^{-1}$, and the non-chiral combination xyxy-xyyx spectra have extended red peaks at that center. These peaks centered at $52\ 000\ \text{cm}^{-1}$ correspond to the maxima in the LA signal displayed at the top row. The yellow cross-peaks in both non-chiral spectra correspond to the pairs of dipole-dipole interactions.

of the time delays $t_1 \rightarrow \Omega_1$ and $t_3 \rightarrow \Omega_3$ (Figure 2). The time delay t_2 is fixed to zero, avoiding energy transfer processes between excited states. Depending on the polarization of the lasers (x, y, z), signals can be non-chiral and chiral.⁵⁶ Chiral signals are much more sensitive to the geometry of the protein than the non-chiral signals, but the nonchiral signals are larger in magnitude.

Three non-chiral signals are independent in the dipole approximation: xyxy, xyyx, and xxyy (x and y are the polarizations of the lasers). The linear combination, xxxx = xyxy + xyyx + xxyy, gives an absorptive signal with all four laser polarizations in the same direction. Other combinations can be obtained such as xyxy-xyyx, which eliminates the excited-state population pathways and reveals the pathways for coherent quantum dynamics arising from the off-diagonal crosspeaks in the $(-\Omega_1, \Omega_3)$ signal diagrams. The combination xxyy-xyxy suppresses the pathways with coherence in stimulated emission and highlights the excited-state population dynamics. For $t_2 = 0$, xyxy = xyyx and the combination xyxy-xyyx displays only excited-state absorption. In addition, nine independent chiral signals are possible. The chiral xxxx signal was computed and used earlier in the characterization of secondary structure of proteins.⁶¹

In the current study, three sets of signals are computed: the absorptive non-chiral xxxx, the non-chiral combination xyxy-xyyx, and the chiral xxyy. These signals are most easily related to protein conformation. To achieve these signals and compute the 2DUV spectra, the four lasers are set to pulses of $3754\ \text{cm}^{-1}$ bandwidth centered at $52\ 000\ \text{cm}^{-1}$ (190 nm).⁵⁶

For comparison purposes, all 2D spectra are normalized in a color scale to rank the weak (in blue) and strong (in red) peaks, and plotted on a nonlinear scale that interpolates between logarithmic, for small values, and linear for large values, of the signal intensity. The nonlinear scale is defined as⁶³

$$\arcsin h(cS) = \ln(cS + \sqrt{(1 + c^2 S^2)}) \quad (3)$$

S is the 2D signal and c is a constant factor defined in such a way that, for larger cS , the scale becomes logarithmic, and weak

features are amplified and their resolution enhanced. For $cS < 1$, the scale is linear. In each set of computed signals, the constant factor is fixed.

3. RESULTS

The dock/lock mechanism of the $\text{A}\beta$ amyloid fibrils described in ref 47 has three stages, and the transition between stages coincides with abrupt changes in the number of native hydrogen bonds formed between the monomer and the amyloid fibril (Figure 9 in ref 47). The three distinguishable stages can be described as follows: (a) The monomer initially interacts freely with the amyloid fibril template. (b) The monomer partially locks into the amyloid fibril template by making intermolecular hydrogen bonds along one of its strands, whereas the remaining strand is allowed to move freely. (c) The monomer is fully locked in the fibril conformation and can serve as a template for addition of subsequent monomers.

The simulations suggested that the monomers have no preference for binding to either of the ends of configuration 1 or 2 and the dock/lock mechanism does not depend on the size of the template. However, the simulations presented here show that the formation of hydrogen bonds during the conformational changes of the monomer depends on the initial configuration. The description of this dock/lock mechanism is consistent with experiments on deposition of $\text{A}\beta$ -peptide monomers.^{42,43} Molecular dynamics simulation studies of the oligomerization of the $\text{A}\beta_{(16-22)}$ monomers also indicate that a monomer binds onto a preformed oligomer by forming anti-parallel U-shape sheets via a dock/lock mechanism similar to what experiments reported.⁴⁴

3.1. 2DUV Signals of the Amyloid $\text{A}\beta$ -Peptide Dock/Lock Mechanism at Different Simulation Times. The 2DUV signals at different simulation times provide an avenue to assess the conclusions in ref 47, in terms of the geometry of the dipole-dipole interactions. The simulated 1D and 2DFUV (2D far-ultraviolet) spectra for configurations 1 and 2 are presented here, and Figures S1-S5 are displayed in the Supporting Information. The FUV signals (190–250 nm) originate from the amino-acid residues of peptide backbone

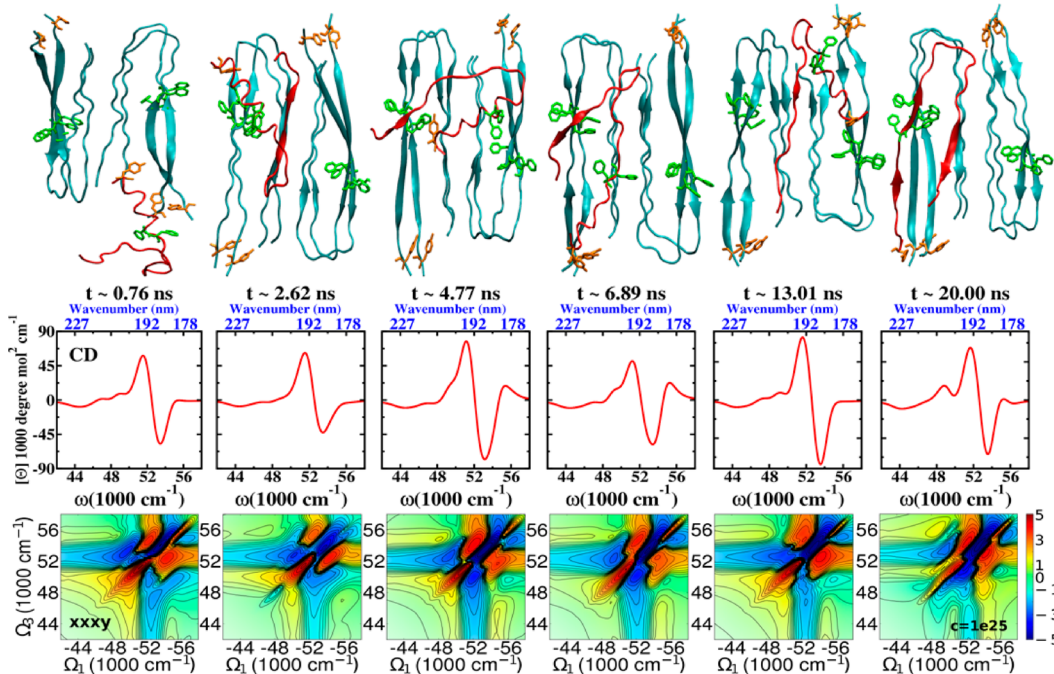


Figure 4. 1D and 2D chiral signals in the FUV for Configuration 1 at different simulation times. Top row: representative snapshots (from ref 47) of $\text{A}\beta_{(9-40)}$ monomer (red) interacting with the amyloid template (blue) at different simulation times. Aromatic residues, Tyr and Phe, are orange and green, respectively. Middle panels: circular dichroism. Bottom panels: 2DFUV chiral xxxx spectra.

$n\pi^*$ and $\pi\pi^*$ transitions and are sensitive to secondary structure. The aromatic residues also contribute to the FUV signal.

The LA signals of configurations 1 and 2 are displayed in Figures 3 and S1 (Supporting Information) (top panels) at six simulation times. All signals share a common peak centered around $52\ 000\ \text{cm}^{-1}$ with modest variations in their profile due to the different stages in the dock/lock process of the $\text{A}\beta_{(9-40)}$ monomer onto the amyloid template. The xxxx signals (Figures 3 and S1 (Supporting Information), middle panels) show a symmetric and elongated blue peak around $52\ 000\ \text{cm}^{-1}$ along the diagonal of the $(-\Omega_1, \Omega_3)$ plots. The diagonal elements correspond to the excitation energies, and their line shapes show lifetimes and couplings to the dipole–dipole interactions. Off-diagonal elements on the $(-\Omega_1 \neq \Omega_3)$ maps are cross-peak signals that carry information about couplings and correlations at different states. Other non-chiral signal combinations enhance some cross-peak signals not observed in the xxxx signals. The combination xyxy–xyyx displayed at the bottom of Figures 3 and S1 (Supporting Information) shows some off-diagonal asymmetric shapes that indicate weak correlations between modes. Because we set $t_2 = 0$, all the signals display excited states absorption. The combination xyxy–xyyx for both configurations displays changes in their cross-peaks in time. The signal in configuration 2 displays a split in the peak at $52\ 000\ \text{cm}^{-1}$ at all times.

The circular dichroism (CD) and the xxxx signals, which reveal the secondary structure chirality, are described below. The CD signal of configurations 1 and 2 at six simulation times are shown in Figures 4 and S2 (Supporting Information) (middle panels), respectively. Absorptions at 240 nm and below are due mainly to two backbone transitions in the peptide groups: A strong peak around 190 nm from $\pi\pi^*$ transitions and a weak but broad plateau due to the $n\pi^*$ transition around 220 nm. The $\text{A}\beta_{(9-40)}$ monomers in the amyloid template in

configuration 1 are predominantly U-shape hairpins and β -strands. The contribution to the changes in the CD signals comes from the conformational changes of the free $\text{A}\beta_{(9-40)}$ monomer during the dock/lock process onto the amyloid template. The changes in the intensity around 190 nm ($52\ 000\ \text{cm}^{-1}$) and 220 nm ($46\ 000\ \text{cm}^{-1}$) come from the interaction between the monomer and the template by hydrogen-bond formation, electrostatic contacts between charged residues, and transitions from aromatic residues.⁵⁶

An extension of the CD signals are the xxxx signals, shown in Figures 4 and S2 (Supporting Information) (bottom panels). Signals in both configurations show two common peaks along the diagonal of the $(-\Omega_1, \Omega_3)$ map: A strong peak around $52\ 000\ \text{cm}^{-1}$ and a weaker one at $54\ 000\ \text{cm}^{-1}$, which are characteristic of a fibrillar structure.⁵¹ Off-diagonal peaks describe the local dynamics of the system and the coupling between amide groups of the backbone.

For configuration 1, the xxxx signal at $t \sim 0.76\ \text{ns}$ (Figure 4, first left column, bottom panel) shows an asymmetric butterfly shape with peaks at $48\ 000$ and $56\ 000\ \text{cm}^{-1}$ that indicate aromatic coupling transitions originating mainly from Phe residues of the monomers in the amyloid stacking of the template (top of Figure 4). From $t \sim 0.76\ \text{ns}$ to $t \sim 6.89\ \text{ns}$, the single monomer interacts weakly with the template and can still move and freely change its position. The 2DFUV xxxx signals (bottom of Figure 4) reflect these changes. The peak at $56\ 000\ \text{cm}^{-1}$ observed at $t \sim 0.76\ \text{ns}$ disappears at $t \sim 2.62\ \text{ns}$ but reappears at $t \sim 4.77\ \text{ns}$. Similarly, the peak at $48\ 000\ \text{cm}^{-1}$ almost disappears at $t \sim 2.62\ \text{ns}$ but reappears, although weakened, at $t \sim 4.77\ \text{ns}$ and $t \sim 6.89\ \text{ns}$. During these times, the coupling interactions, Phe-Tyr and Tyr-Tyr, between the free monomer and the amyloid template occur (top of Figure 4). The CD spectrum at $t \sim 6.89\ \text{ns}$ (Figure 4, fourth left column, middle panel) has a lower peak at $52\ 000\ \text{cm}^{-1}$ and a plateau around 220 nm, which indicates that the free monomer

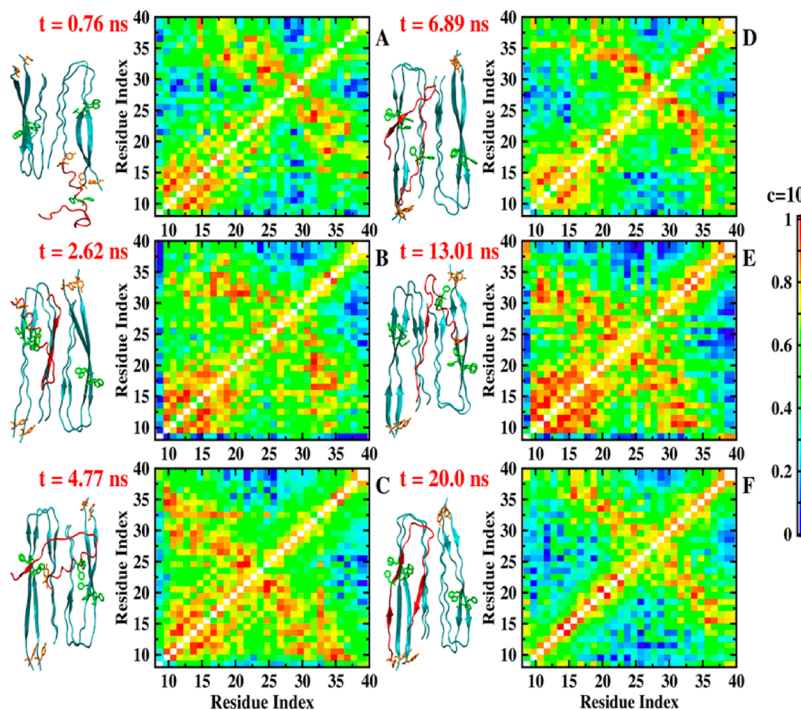


Figure 5. Maps A–F showing the average chirality factor $\langle \text{CF}(m,n) \rangle$ (eq 4) for $\pi\pi^*$ transitions for Configuration 1 at different simulation times, indicated at the left of each map. A representative snapshot (obtained from ref 47) of the $\text{A}\beta_{(9-40)}$ monomer (red) interacting with the amyloid template (blue) for the corresponding time, is also shown at the left of each map. Axes in each map correspond to the amino-acid residue index. Equation 3 was used with a fixed value for c to highlight the contribution of a pair of amino-acid residues to the chirality factor .

has formed a U-shaped hairpin and is partially bound onto one of the stacks in the amyloid template making Phe-Tyr coupling interactions. This occurs similarly at $t \sim 13.01$ ns. Accordingly, the signal displays strong peaks at 48 000 and 56 000 cm^{-1} (Figure 4, bottom of fifth column from the left). The free segment, Gly9-Asp23, is still unbound and free to move. At $t \sim 20$ ns, this free segment finally binds to the template with the fibrillar conformation, locking the monomer and allowing it to form Phe-Phe and Tyr-Tyr interactions with the template.

For configuration 2, the $xxxx$ signals display a different profile. At $t \sim 0.05$ ns (Figure S2 (Supporting Information), first column from the left), the main contribution to the signal comes from the template because the free monomer has an extended shape and is far from the template. The signal displays peaks at 48 000 and 56 000 cm^{-1} due to the interactions between the aromatic residues. Within the times $t \sim 0.27$ ns and $t \sim 3.76$ ns (Figure S2 (Supporting Information), second to fourth columns from the left), conformational changes in the monomer are reflected in the $xxxx$ signal. At $t \sim 0.27$ ns, the Ala30-Val40 segment of the free monomer interacts with the template allowing Phe-Tyr coupling interactions that are reflected in the $xxxx$ signal as several cross-peaks along the diagonal. At $t \sim 1.45$ ns, the monomer binds partially to the template, and the signal displays peaks at 48 000, 52 000, and 56 000 cm^{-1} . At $t \sim 3.76$ ns, the signal exhibits a butterfly-like shape and the monomer forms a bulky structure and interacts with the amyloid template. At $t \sim 16.75$ ns, the monomer starts to bind to the template. Phe-Phe, and Tyr-Tyr couplings are present, and the butterfly-like shape appears in the signal. At $t \sim 20$ ns, the monomer binds and locks fully to the template, and the $xxxx$ signal displays diffused peaks along the diagonal. The signal still preserves the characteristic peaks at 48 000,

52 000, and 56 000 cm^{-1} , but the profile of the signal differs from that in configuration 1.

3.2. Chirality Factor and the Secondary Structure at Different Simulation Times. From the 2DUV spectroscopy point of view, changes in the conformation of the monomer are associated with changes in the relative orientations of the transition dipole moments in the residues. These can be used to characterize the secondary structure by measuring the interactions between the transition dipole moments during different orientations. For example, the contribution of pairs of amino-acid residues to the chiral signals can be characterized quantitatively in terms of the average chirality factor $\langle \text{CF}(m,n) \rangle$:⁵²

$$\langle \text{CF}(m,n) \rangle = \sum_{i=1}^N |\Psi_{m_e}^i \Psi_{n_e}^i \mathbf{R}_{mn}^i (\mu_m^i \times \mu_n^i)| \quad (4)$$

where $i = 1, \dots, N$ are the indices of the snapshots of a set in a simulation time interval. m and n are the indices of the local amino-acid residue mode ($n\pi^*$ and $\pi\pi^*$), $\Psi_{m_e}^i$ is the eigenstate wave function e of the localized amino-acid residue m , \mathbf{R}_{mn}^i is the distance between the positions of the two transition electric dipole moments μ_m^i and μ_n^i . The CD signal is obtained by summing over all the eigenstates at one frequency, $S(e) = \sum_{i=1}^N \Psi_{m_e}^i \Psi_{n_e}^i \mathbf{R}_{mn}^i (\mu_m^i \times \mu_n^i)$. In the UV regime, each amino-acid residue undergoes two transitions, $n\pi^*$ and $\pi\pi^*$, each of which carries the same conformational information. For this study, the $\pi\pi^*$ transitions of each amide group were used to compute the $\langle \text{CF}(m,n) \rangle$ maps, and each pair of amino acids is associated with formation of secondary structure in the $\text{A}\beta_{(9-40)}$ monomer.

The $\langle \text{CF}(m,n) \rangle$ maps of the monomer for configuration 1 at different simulation times are displayed in Figure 5. At $t \sim 0.76$ ns (Figure 5A), a long anti-diagonal structure is displayed on

the map, characteristic of anti-parallel β -sheets (as in contact distance maps). This indicates the presence of a turn around Asn27, which brings the Gln15-Gly25 and Ala30-Val36 segments close to each other and in anti-parallel orientation. This structure persists at all times, with only the turn region shifting slightly. Accordingly, the anti-diagonal structure on the maps also persists at all times, except that it moves toward right or left depending on the position of the turn.

Another persistent feature is the region along the diagonal in the lower left corner of all the maps between $t \sim 0.76$ ns and $t \sim 13.01$ ns (Figure 5, panels A to E). It indicates that the dipole moment vectors are parallel, typical of α -helices. This is consistent with the presence of an α -helix formed by the Gly9-Asp23 segment whose length changes in time as observed in each panel in Figure 5.

At $t \sim 20$ ns (Figure 5F), the monomer finally docks adopting the fibrillar conformation. The chirality factor map clearly shows the geometrical configuration of the fibril. The α -helix has disappeared and so has the diagonal structure in the lower left corner of the map. The Gly9-Asp23 and Ala30-Val40 segments lie in anti-parallel orientation, resembling a β -hairpin. Their interaction is seen in the signal from the turn region as a high-chirality region (blue) intersecting the diagonal around residue Asn27.

The chirality factor maps for configuration 2 at different simulation times are shown in Figure S3 (Supporting Information). Between $t \sim 0.05$ and $t \sim 1.45$ ns (Figure S3, panels A–C, Supporting Information), the segment Gly9-Asp23 of the free monomer exhibits an α -helical-shape, which is consistent with the red region along the diagonal in the lower left corner of the maps. At $t \sim 1.45$ ns, the segment Ala30-Val40 of the monomer interacts with one monomer from the template and gradually starts bending to form a turn around residue Leu34, which is reflected in the map by the region intersecting the diagonal around residue Leu34 (Figure S3C, Supporting Information). At $t \sim 3.76$ ns (Figure S3D, Supporting Information), the chirality map displays an irregular profile because the free monomer forms a bulky structure, and π -stacking interactions between aromatic residues from the free monomer and the template are present. At $t \sim 16.75$ ns, the segment Gly9-Asp23 of the free monomer binds partially to the template and the remaining portion (Val24-Val40) moves freely with all its transition dipole moments interacting with each other in all directions (Figure S3E, Supporting Information). At $t \sim 20.0$ ns (Figure S3F, Supporting Information), the monomer finally docks to the template, and the profile of the $\langle CF(m,n) \rangle$ map is similar to that in Figure 5F. A red segment intersects the diagonal around residue Ser26, indicating the formation of a turn at this location and interactions between the Gly9-Asp23 and Ala30-Val40 segments.

3.3. Sensitivity Analysis of the 2DUV Spectra. The 2DUV signals reported in section 3.1 depend strongly on the initial configurations of the incoming monomer. These signals arise mainly from the complex (monomer + amyloid template). For configurations 1 and 2, a sensitivity analysis was performed to determine which component (monomer or amyloid template) is more sensitive in making the larger changes in the signals.

Sensitivity analysis of the signals consists of dissecting the 2DUV signal into the following parts:

$$S_{\text{complex}} = S_{\text{template}} + S_{\text{monomer}} + \Delta S \quad (5)$$

where S_A is the 2DUV signal of component A labeled as complex, template, and monomer, respectively, in eq 5. Because of the coupling elements in the Hamiltonian, the total signal, S_{complex} , is not the addition of the signal of each component. Therefore, a factor ΔS is included and used to weight the contribution of each component to the total spectrum. The non-chiral signals $S^{(xxxx)}$ of each component for configurations 1 and 2 are shown in Figures S4 and S5 (Supporting Information), respectively. The $S^{(xxxx)}$ signals at different simulation times (see the columns of Figures S4 and S5, Supporting Information) coming from the amyloid template and the monomer for both configurations show that the main contribution to the $S^{(xxxx)}$ complex comes strongly from the amyloid template rather than from the monomer, where the latter is the component with the largest conformational changes over time. The dynamics of these signals for both configurations (Figures S4 and S5, Supporting Information) can be observed in the changes of ΔS at different simulation times.

For configuration 1 (Figure S4, Supporting Information), at $t \sim 0.76$ ns, the monomer is initially far from the template, and the coupling terms of the monomer and the template display two well-separated positive (yellow) and negative (blue) cross-peaks around 52 000 and 54 000 cm^{-1} (Figure S4, Supporting Information, ΔS). At $t \sim 2.76$ ns, the negative peak elongates sharply along the diagonal, which indicates that the coupling terms have a broader range in frequency due to the fact that the monomer binds partially as a β -sheet to the template with the hairpin in the opposite orientation. The positive cross-peak signals remain unaltered.

Later at $t \sim 4.77$ ns, ΔS displays both cross-peaks elongated uniformly along the diagonal. Here, the monomer forms a hairpin shape with some helical structure. At $t \sim 6.89$ ns, a segment of the monomer binds to one of the already-stacked monomers in the template, and the cross-peaks spread out broadly around 52 000 cm^{-1} . At $t \sim 13.01$ ns, the monomer has a hairpin shape and partially unlocks from the original stack, and ΔS exhibits a similar behavior as at early times, with the negative cross-peak signals spreading out broader than the positive cross-peak signals. At $t \sim 20.0$ ns, when the monomer binds fully to the template, ΔS displays its cross-peaks in the entire FUV range.

For configuration 2 (Figure S5, Supporting Information), ΔS at different times reveals a distinct pathway. At early times, $t \sim 0.05$ ns and $t \sim 0.27$ ns, two cross-peaks are displayed around 52 000 and 54 000 cm^{-1} as in configuration 1. The monomer binds partially with one of the stacks at $t \sim 1.45$ ns and $t \sim 3.76$ ns. At that time interval, the negative cross-peak spreads out and becomes broader and more delocalized than the positive peak. Later in time, at $t \sim 16.75$ ns the monomer binds to the template as a U-shape hairpin, and ΔS exhibits an elongated negative cross-peak along the diagonal, which persists once the monomer binds fully to the template at $t \sim 20.0$ ns.

Thus, the sensitivity analysis has helped to extract information from the nonchiral signals about the changes in the cross-peaks at different times that are usually seen in the chiral signals.

4. DISCUSSION AND CONCLUSIONS

2DUV spectra at specific times during the amyloid assembly reveal that the local dynamics depend on the initial condition of the monomer-template configuration. Rojas et al.⁴⁷ showed that both initial configurations are valid for the amyloid assembly and did not find evidence of preference of one configuration

over the other. Although both configurations share a common two-stage dock/lock mechanism as indicated in ref 47, the 2DFUV chiral *xxxx* signals at various times indicate distinct signal pathways (Figures 4 and S2, Supporting Information). In configuration 1 the free monomer seems to follow a highly and steadily cooperative folding process, whereas in configuration 2 the *xxxx* signals display abundant cross-peaks, indicating local strong coupling in certain pairs of residues in the monomer.

In silico studies of fragments or full-length $\text{A}\beta$ -peptides have been reported.^{32–41} These studies used intramolecular average residue-contact maps or atom-distance-based plots that usually provide a general overview of the secondary structure and critical contacts formed during folding at a given temperature. Here, the characteristics of the local dynamics in the amino-acid backbone residues are well represented by the average chirality factor maps that preserve the general description of the secondary structure and reveal that the free monomer displays a more localized dynamics in configuration 1 than in configuration 2. In configuration 1, segments Gly9-Gln15, Leu17-Ala21, and Ile31-Val36 of the monomer are dominant portions of the sequence that lead to monomer folding and cooperate with each other in the formation of secondary structure. In configuration 2, the formation of helical and β -strand structures seems to be slower, less cooperative and with more delocalized dynamics than in configuration 1, at least at early times.

In the final locking step, both configurations display similar profiles in the chirality factor map. The Leu17-Ala21 and Ile31-Val36 segments form β -strands connected by a hairpin loop. The Leu17-Ala21 and Ile31-Val36 segments of the free monomer in configuration 1 display a uniform contribution to the chirality whereas, in configuration 2, some pairs of residues, especially the aromatics Phe19 and Phe20, make the strongest contribution to the chirality.

These results agree with experimental studies of $\text{A}\beta_{(10-35)}$ fragments. Studies by Lee et al.⁶⁴ demonstrated that $\text{A}\beta_{(10-35)}$ fragments populate collapsed coil conformations under physiological conditions, under which the hydrophobic amino-acid residues L17-A21 formed a well-structured core. Benzingier et al.^{65,66} used solid state NMR on fibrils of $\text{A}\beta_{(10-35)}$ peptides and found that the full length $\text{A}\beta$ peptides adopt the structure of an extended parallel in-register β -sheet at pH 7.4. Also, they demonstrated that structural transitions from α -helix to β -sheet were observed at residues Phe19 and Phe20 by using peptides with ¹³C incorporated at the carbonyl position of adjacent amino acids, Val18 and Phe19, respectively.

Finally, the analyzed 2DUV spectra can be used to characterize the mechanism of fibril elongation of the $\text{A}\beta$ amyloid fibrils in great detail, and clearly discriminate the different dock/lock pathways which a single monomer takes to bind to a fibril template. The results shown here indicate that it is possible to correlate the different conformations that the monomer adopts with the 2DFUV signals, especially with the chiral signals (Figures 4 and S2, Supporting Information) and the chirality factors (Figure 5 and S3, Supporting Information). The 2DUV spectra analyzed here have provided confirming details of the structures in the resulting docking events described in ref 47. Recent applications of experimental and simulated spectroscopy in the infrared regime such as 2DIR and FTIR have been found to be promising for proteins and higher-order structures such as amyloid fibrils, Ras proteins, and the photosystem. They exhibit ultrafast chemical processes that are sensitive in the infrared regime such as proton transport,

vibrational dynamics, secondary structure stability, and protein activation, and their detailed characterization has helped to understand macroscopical processes in proteins.^{67–72}

ASSOCIATED CONTENT

S Supporting Information

1D and 2D spectra in the FUV regime for configuration 2, maps of the average chirality factor for configuration 2, and components of the 2DFUV non-chiral *xxxx* signal dissection for configurations 1 and 2. This material is available free of charge via the Internet at <http://pubs.acs.org>.

AUTHOR INFORMATION

Corresponding Author

*E-mail: alamng@uci.edu, alfonso.lam@gmail.com.

Notes

The authors declare no competing financial interest.

ACKNOWLEDGMENTS

This work was supported by the National Institutes of Health (Grants GM059230, GM091364, AI83206, and GM14312), and the National Science Foundation (Grants CHE-1058791 and MCB-1019767). The MD simulations were conducted by using the resources of the 616-processor Beowulf cluster at the Baker Laboratory of Chemistry, Cornell University. The 2DUV spectra were computed in the Green Planet supercluster at the University of California Irvine.

REFERENCES

- (1) Lorenzo, A.; Yuan, M.; Zhang, Z.; Paganetti, P. A.; Sturchler-Pierrat, C.; Staufenbiel, M.; Mautino, J.; Vigo, F. S.; Sommer, B.; Yankner, B. A. *Nat. Neurosci.* **2000**, *3*, 460–464.
- (2) Walsh, D. M.; Klyubin, I.; Fadeeva, J. V.; Cullen, W. K.; Anwy, R.; Wolfe, M. S.; Rowan, M. J.; Selkoe, D. J. *Nature* **2002**, *416*, 535–539.
- (3) Selkoe, D. J. *Physiol. Rev.* **2001**, *81*, 741–766.
- (4) Kirkadze, M. D.; Bitan, G.; Teplow, D. B. *J. Neurosci. Res.* **2002**, *69*, 567–577.
- (5) Hardy, J.; Selkoe, D. J. *Science* **2002**, *297*, 353–356.
- (6) Hardy, J. *Neurobiol. Aging* **2002**, *23*, 1073–1074.
- (7) Haass, C.; Selkoe, D. J. *Nat. Rev. Mol. Cell Biol.* **2007**, *101*–112.
- (8) Nelson, R.; Sawaya, M. R.; Balbirnie, M.; Madsen, A. O.; Riek, C.; Grothe, R.; Eisenberg, D. *Nature* **2005**, *435*, 773–778.
- (9) Sawaya, M. R.; Sambashivan, S.; Nelson, R.; Ivanova, M. I.; Sievers, S. A.; Apostol, M. I.; Thompson, M. J.; Balbirnie, M.; Wilzus, J. J. W.; McFarlane, H. T.; et al. *Nature* **2007**, *447*, 453–457.
- (10) Colletier, J. P.; Laganowsky, A.; Landau, M.; Zhao, M. L.; Soria, A. B.; Goldschmidt, L.; Flot, D.; Cascio, D.; Sawaya, M. R.; Eisenberg, D. *Proc. Natl. Acad. Sci. U. S. A.* **2011**, *108*, 16938–16943.
- (11) Crescenzi, O.; Tomaselli, S.; Guerrini, R.; Salvatori, S.; D’Ursi, A. M.; Temussi, P. A.; Picone, D. *Eur. J. Biochem.* **2002**, *269*, 5642–5648.
- (12) Petkova, A. T.; Ishii, Y.; Balbach, J. J.; Antzutkin, O. N.; Leapman, R. D.; Delaglio, F.; Tycko, R. *Proc. Natl. Acad. Sci. U. S. A.* **2002**, *99*, 16742–16747.
- (13) Petkova, A. T.; Leapman, R. D.; Guo, Z.; Yau, W.-M.; Mattson, M. P.; Tycko, R. *Science* **2005**, *307*, 262–265.
- (14) Petkova, A. T.; Yau, W.-M.; Tycko, R. *Biochemistry* **2006**, *45*, 498–512.
- (15) Paravastu, A.; Leapman, R. D.; Yau, W.; Tycko, R. *Proc. Natl. Acad. Sci. U. S. A.* **2008**, *105*, 18349–18354.
- (16) Tycko, R.; Sciarretta, K. L.; Orgel, J. P. R. O.; Meredith, S. C. *Biochemistry* **2009**, *48*, 6072–6084.
- (17) Lührs, T.; Ritter, C.; Adrian, M.; Riek-Lohr, D.; Bohrmann, B.; Döbeli, H.; Schubert, D.; Riek, R. *Proc. Natl. Acad. Sci. U. S. A.* **2005**, *102*, 17342–17347.

- (18) Walsh, D. M.; Lomakin, A.; Benedek, G. B.; Condron, M. M.; Teplow, D. *J. Biol. Chem.* **1997**, *272*, 22364–22372.
- (19) Lazo, N. D.; Downing, D. T. *J. Pept. Res.* **1999**, *53*, 633–640.
- (20) Kirkitadze, M. D.; Condron, M. M.; Teplow, D. B. *J. Mol. Biol.* **2001**, *312*, 1103–1119.
- (21) Kayed, R.; Head, E.; Thompson, J. L.; McIntire, T. M.; Milton, S. C.; Cotman, C. W.; Glabe, C. G. *Science* **2003**, *300*, 486–489.
- (22) Bitan, G.; Kirkitadze, M. D.; Lomakin, A.; Vollmers, S. S.; Benedek, G. B.; Teplow, D. B. *Proc. Natl. Acad. Sci. U. S. A.* **2003**, *100*, 330–335.
- (23) Bitan, G.; Vollmers, S.; Teplow, D. B. *J. Biol. Chem.* **2003**, *278*, 34882–34889.
- (24) Bitan, G.; Tarus, B.; Vollmers, S. S.; Lashuel, H. A.; Condron, M. M.; Straub, J. E.; Teplow, D. B. *J. Am. Chem. Soc.* **2003**, *125*, 15359–15365.
- (25) Klein, W. L.; Stine, W. B.; Teplow, D. B. *Neurobiol. Aging* **2004**, *25*, 569–580.
- (26) Lazo, N. D.; Grant, M. A.; Condron, M. C.; Rigby, A. C.; Teplow, D. B. *Protein Sci.* **2005**, *14*, 1581–1596.
- (27) Glabe, C. G. *Subcell Biochem.* **2005**, *38*, 167–177.
- (28) Cheng, I. H.; Scearce-Levie, K.; Legleiter, J.; Palop, J. J.; Gerstein, H.; Bien-Ly, N.; Puolivili, J.; Lesne, S.; Ashe, K. H.; Muchowski, P. J.; et al. *J. Biol. Chem.* **2007**, *282*, 23818–23828.
- (29) Lim, K. H.; Colver, H. H.; Le, Y. T. H.; Nagchowdhuri, P.; Kenney, J. M. *Biochem. Biophys. Res. Commun.* **2006**, *353*, 443–449.
- (30) Jarret, J. T.; Berger, E. P.; Lansbury, P. T. *J. Ann. N. Y. Acad. Sci.* **1993**, *695*, 144–148.
- (31) Jarret, J. T.; Berger, E. P.; Lansbury, P. T. *Biochemistry* **1993**, *32*, 4693–4697.
- (32) Massi, F.; Peng, J. W.; Lee, J. P.; Straub, J. E. *Biophys. J.* **2001**, *80*, 31–44.
- (33) Borreguero, J. M.; Urbanc, B.; Lazo, N. D.; Buldyrev, S. V.; Teplow, D. B.; Stanley, H. E. *Proc. Natl. Acad. Sci. U. S. A.* **2005**, *102*, 6015–6020.
- (34) Wei, G.; Jewett, A. I.; Shea, J.-E. *Phys. Chem. Chem. Phys.* **2010**, *12*, 3622–3629.
- (35) Nguyen, P. H.; Li, M. S.; Derreumaux, P. *Phys. Chem. Chem. Phys.* **2011**, *13*, 9778–9788.
- (36) Urbanc, B.; Cruz, L.; Yun, S.; Buldyrev, S. V.; Bitan, G.; Teplow, D. B.; Stanley, H. E. *Proc. Natl. Acad. Sci. U. S. A.* **2004**, *101*, 17345–17350.
- (37) Lam, A.; Urbanc, B.; Borreguero, J.; Lazo, N. D.; Teplow, D. B.; Stanley, H. E. *Proc. 2006 Int. Conf. Bioinformatics Comput. Biol.* **2006**, *1*, 322–328.
- (38) Baumketner, A.; Bernstein, S. L.; Wyttenbach, T.; Bitan, G.; Teplow, D. B.; Bowers, M. T.; Shea, J.-E. *Protein Sci.* **2006**, *15*, 420–428.
- (39) Lam, A. R.; Teplow, D. B.; Stanley, H. E.; Urbanc, B. *J. Am. Chem. Soc.* **2008**, *130*, 17413–17422.
- (40) Kent, A.; Jha, A. K.; Fitzgerald, J. E.; Freed, K. F. *J. Phys. Chem. B* **2008**, *112*, 6175–6186.
- (41) Sgourakis, N. G.; Yan, Y.; McCallum, S. A.; Wang, C.; Garcia, A. E. *J. Mol. Biol.* **2007**, *368*, 1448–1457.
- (42) Esler, W. P.; Stimson, E. R.; Jennings, J. M.; Vinters, H. V.; Ghilardi, J. R.; Lee, J. P.; Mantyh, P. W.; Maggio, J. E. *Biochemistry* **2000**, *39*, 6288–6295.
- (43) Cannon, M. J.; Williams, A. D.; R., W.; Myszka, D. G. *Anal. Biochem.* **2004**, *328*, 67–75.
- (44) Massi, F.; Straub, J. E. *Proteins: Struct., Funct. Genet.* **2001**, *42*, 217–229.
- (45) Nguyen, P. H.; Li, M. S.; Stock, G.; Straub, J. E.; Thirumalai, D. *Proc. Natl. Acad. Sci. U. S. A.* **2007**, *104*, 111–116.
- (46) O'Brien, E. P.; Okamoto, Y.; Straub, J. E.; Brooks, B. R.; Thirumalai, D. *J. Phys. Chem. B* **2009**, *113*, 14421–14430.
- (47) Rojas, A.; Liwo, A.; Browne, D.; Scheraga, H. A. *J. Mol. Biol.* **2010**, *404*, 537–552.
- (48) Smith, A. W.; Tokmakoff, A. *J. Chem. Phys.* **2007**, *126*, 045109–1–10.
- (49) Kim, Y. S.; Liu, L.; Axelsen, P. H.; Hochstrasser, R. M. *Proc. Natl. Acad. Sci. U. S. A.* **2008**, *105*, 7720–7725.
- (50) Strasfeld, D. B.; Ling, Y. L.; Shim, S.-H.; Zanni, M. T. *J. Am. Chem. Soc.* **2008**, *130*, 6698–6699.
- (51) Shim, S.-H.; Gupta, R.; Ling, Y. L.; Strasfeld, D. B.; Raleigh, D. P.; Zanni, M. T. *Proc. Natl. Acad. Sci. U. S. A.* **2009**, *106*, 6614–6619.
- (52) Zhuang, W.; Sgourakis, N. K.; Zhenyu, L.; Garcia, A.; Mukamel, S. *Proc. Natl. Acad. Sci. U. S. A.* **2010**, *107*, 15687–15692.
- (53) Remorino, A.; Korendovych, I. V.; Wu, Y. B.; DeGrado, W. F.; Hochstrasser, R. M. *Science* **2011**, *332*, 1206–1209.
- (54) West, B. A.; Womick, J. M.; Moran, A. M. *J. Phys. Chem. A* **2011**, *115*, 8630–8637.
- (55) Tseng, C.-H.; Sándor, P.; Kotur, M.; Weinacht, T. C.; Matsika, S. *J. Phys. Chem. A* **2012**, *116*, 2654–2661.
- (56) Jiang, J.; Abramavicius, D.; Bulheller, B. M.; Hirst, J. D.; Mukamel, S. *J. Phys. Chem. B* **2010**, *114*, 8270–8277.
- (57) Abramavicius, D.; Jiang, J.; Bulheller, B. M.; Hirst, J. D.; Mukamel, S. *J. Am. Chem. Soc.* **2010**, *132*, 7769–7775.
- (58) Jiang, J.; Abramavicius, D.; Falvo, C.; Bulheller, B. M.; Hirst, J. D.; Mukamel, S. *J. Phys. Chem. B* **2010**, *114*, 12150–12156.
- (59) Lam, A.; Jiang, J.; Mukamel, S. *Biochemistry* **2011**, *50*, 9809–9816.
- (60) Liwo, A.; Czaplewski, C.; Pillardy, J.; Scheraga, H. A. *J. Chem. Phys.* **2001**, *115*, 2323–2347.
- (61) Abramavicius, D.; Palmieri, B.; Voronine, D. V.; Sanda, F.; Mukamel, S. *Chem. Rev.* **2009**, *109*, 2350–2408.
- (62) Bulheller, B. M.; Rodger, A.; Hirst, J. D. *Phys. Chem. Chem. Phys.* **2007**, *9*, 2020–2035.
- (63) Read, E. L.; Engel, G. S.; Calhoun, T. R.; Mancal, T.; Ahn, T. K.; Blankenship, R. E.; Fleming, G. R. *Proc. Natl. Acad. Sci. U. S. A.* **2007**, *104*, 14203–14208.
- (64) Lee, J. P.; Stimson, E. R.; Ghilardi, J. R.; Mantyh, P. W.; Lu, Y. A.; Felix, A. M.; Llanos, W.; Behbin, A.; Cummings, M.; Crikeling, M. V.; et al. *Biochemistry* **1995**, *34*, 5191–5200.
- (65) Benzinger, T. L.; Gregory, D. M.; Burkoth, T. S.; Miller-Auer, H.; Lynn, D. G.; Botto, R. E.; Meredith, S. C. *Proc. Natl. Acad. Sci. U. S. A.* **1998**, *95*, 13407–13412.
- (66) Benzinger, T. L.; Gregory, D. M.; Burkoth, T. S.; Miller-Auer, H.; Lynn, D. G.; Botto, R. E.; Meredith, S. C. *Biochemistry* **2000**, *39*, 3491–3499.
- (67) Smith, A. W.; Lessing, J.; Ganim, Z.; Peng, C. S.; Tokmakoff, A.; Roy, S.; Jansen, T. L. C.; Knoester, J. *J. Phys. Chem. B* **2010**, *114*, 10913–10924.
- (68) Kobus, M.; Nguyen, P. H.; Stock, G. *J. Chem. Phys.* **2010**, *133*, 034512.
- (69) Liang, C. W.; Jansen, T. L. C.; Knoester, J. *J. Chem. Phys.* **2011**, *134*, 044502.
- (70) Wang, L.; Middleton, C. T.; Singh, S.; Reddy, A. S.; Woys, A. M.; Strasfeld, D. B.; Marek, P.; Raleigh, D. P.; de Pablo, J. J.; Zanni, M. T.; et al. *J. Am. Chem. Soc.* **2011**, *133*, 16062–16071.
- (71) Rudack, T.; Xia, F.; Schlitter, J.; Kotting, C.; Gerwert, K. *Proc. Natl. Acad. Sci. U. S. A.* **2012**, *109*, 15295–15300.
- (72) Suzuki, H.; Sugiura, M.; Noguchi, T. *Biochemistry* **2012**, *51*, 6776–6785.